Supporting Information

In-situ synthesized oxygen-vacancy-rich CuO nanosheet arrays for low-temperature ppb-level NO_2 sensing

Optimization of Hydrothermal Reaction Conditions for CuO Nanosheet Arrays: The hydrothermal reaction temperature and duration were determined based on both literature reports[1] and preliminary experimental results. Previous studies have shown that relatively low hydrothermal temperatures tend to favor the growth of one-dimensional anisotropic CuO structures, whereas the higher temperature used in this work is more conducive to two-dimensional lateral growth. In the preliminary experiments, the CuO samples prepared at 90℃ exhibited relatively low responses and poor selectivity toward NO_2 (Fig. S1). In contrast, the CuO nanosheets synthesized at 120℃ for 12.5, 15, 17.5, and 19 h (Fig. S2) showed higher responses and better selectivity toward NO_2. Therefore, 120℃ was selected as the hydrothermal temperature for constructing CuO nanosheets in this study. The effects of reaction time (12.5, 15, 17.5, and 19 h) on the structure and gas-sensing performance were further investigated. A prolonged hydrothermal duration of 19 h led to increased nanosheet thickness and overgrowth of the nanosheets, resulting in a decline in the NO_2 sensing performance. Within the investigated parameter range, the samples prepared at 120℃ for 12.5, 15, and 17.5 h exhibited better overall performance. Three independent batches of CuO samples were prepared under hydrothermal conditions at 120°C for 15 h, and the SEM (Fig. S3) results showed highly consistent and uniform nanosheet-array morphologies, confirming the good reproducibility of the synthesis process. The present synthesis was conducted on a laboratory small-batch scale, and further optimization of batch size, process reproducibility, and device-to-device consistency will be required for scalable production and practical application.

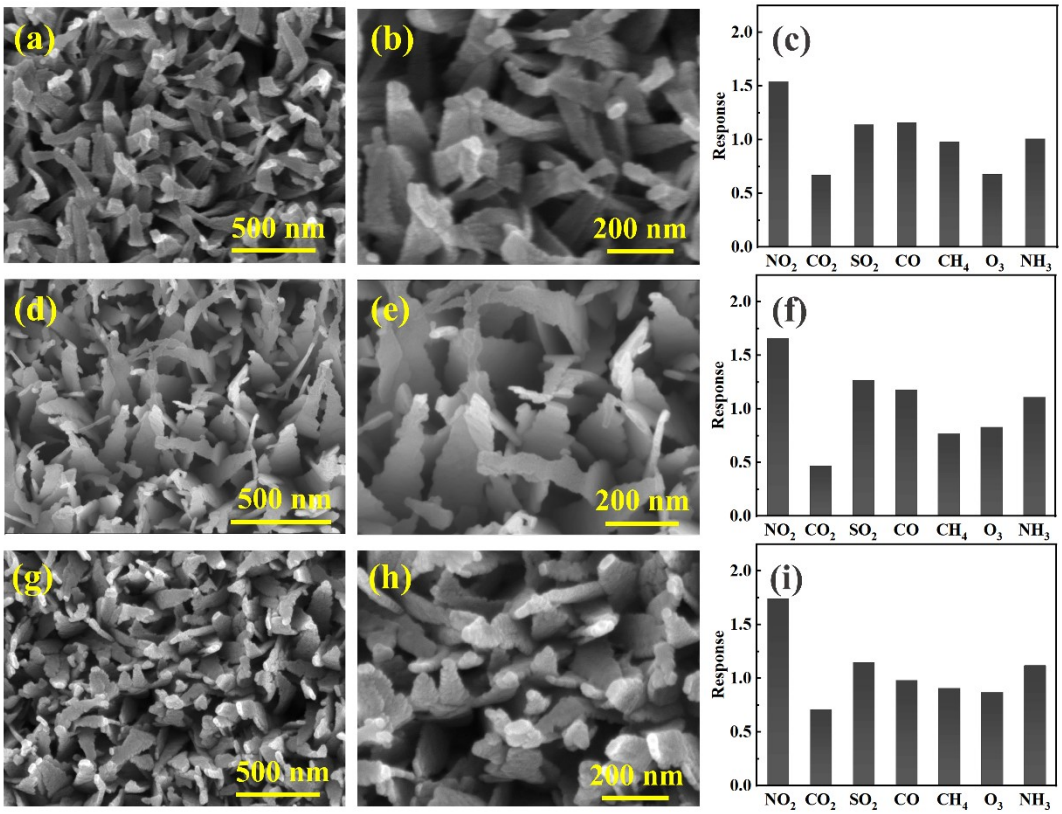

Fig. S1 FESEM images of flakes CuO (a-b) $CuO_{90°C\text{-}12.5\ h}$. (d-e) $CuO_{90°C\text{-}15\ h}$. (g-h) $CuO_{90°C\text{-}17.5\ h}$. (c,f,i) Selectivity of $CuO_{90°C\text{-}12.5\ h}$, $CuO_{90°C\text{-}15\ h}$, and $CuO_{90°C\text{-}17.5\ h}$ sensors to 100 ppb different interfering gases (carbon dioxide, sulfur dioxide, carbon monoxide, methane, ozone, ammonia).

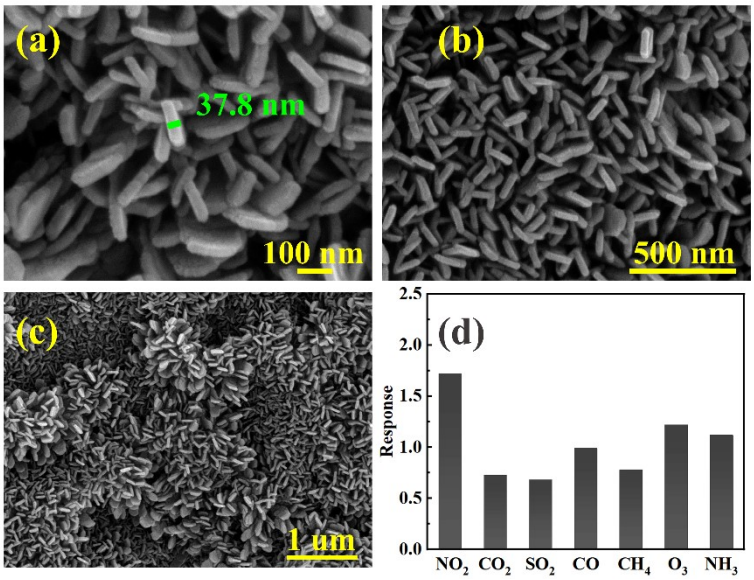

Fig. S2 (a-c) FESEM images of flakes $CuO_{120°C\text{-}19h}$. (b) Selectivity of $CuO_{120°C\text{-}19\ h}$ sensors to 100 ppb different interfering gases (carbon dioxide, sulfur dioxide, carbon monoxide, methane, ozone, ammonia).

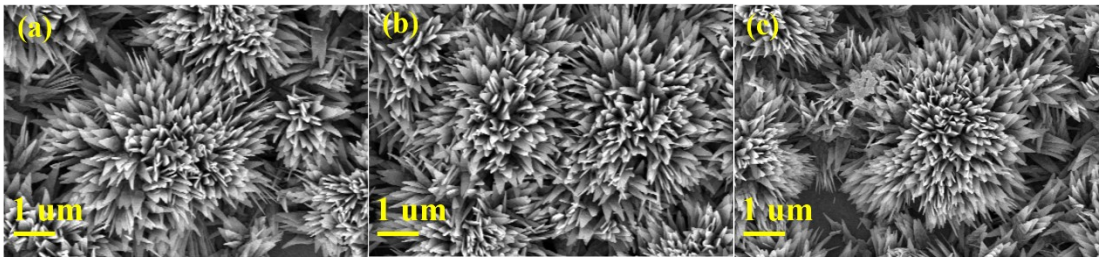

Fig. S3 SEM images of flakes (a) $CuO_{120°C\text{-}15\ h}$-1. (b) $CuO_{120°C\text{-}15\ h}$-2. (c) $CuO_{120°C\text{-}15\ h}$-3.

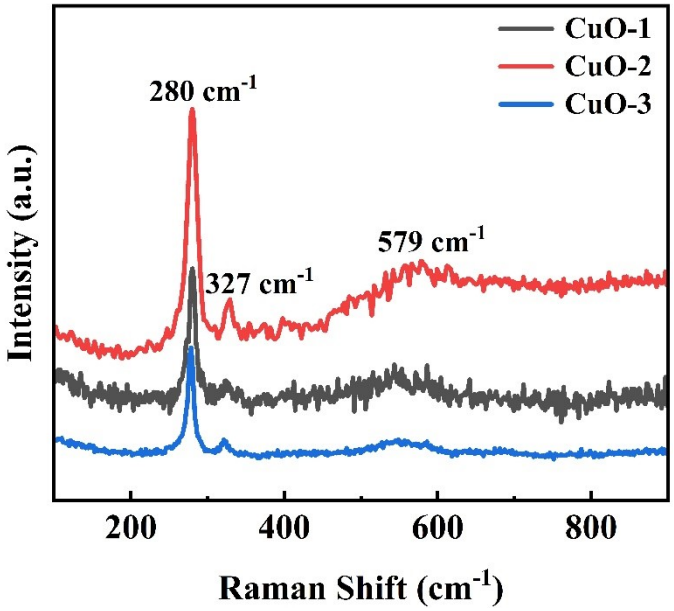

Fig. S4 Raman spectra of CuO-1, CuO-2, and CuO-3.

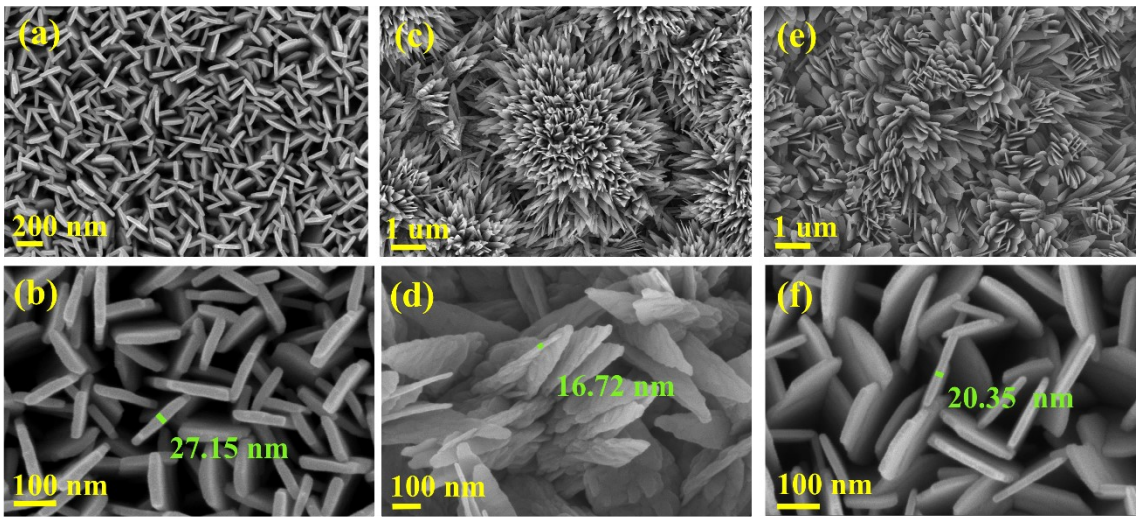

Fig. S5 FESEM images of flakes CuO (a-b) CuO-1. (c-d) CuO-2. (e-f) CuO-3.

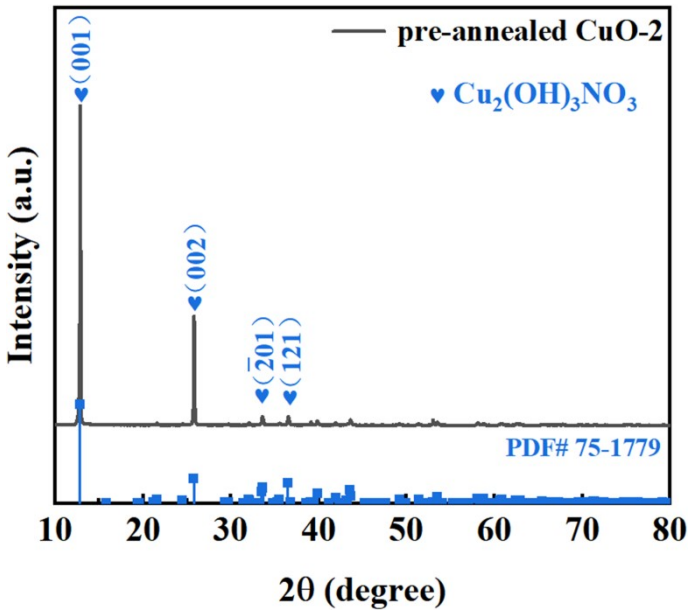

Fig. S6 The XRD pattern of pre-annealed CuO-2.

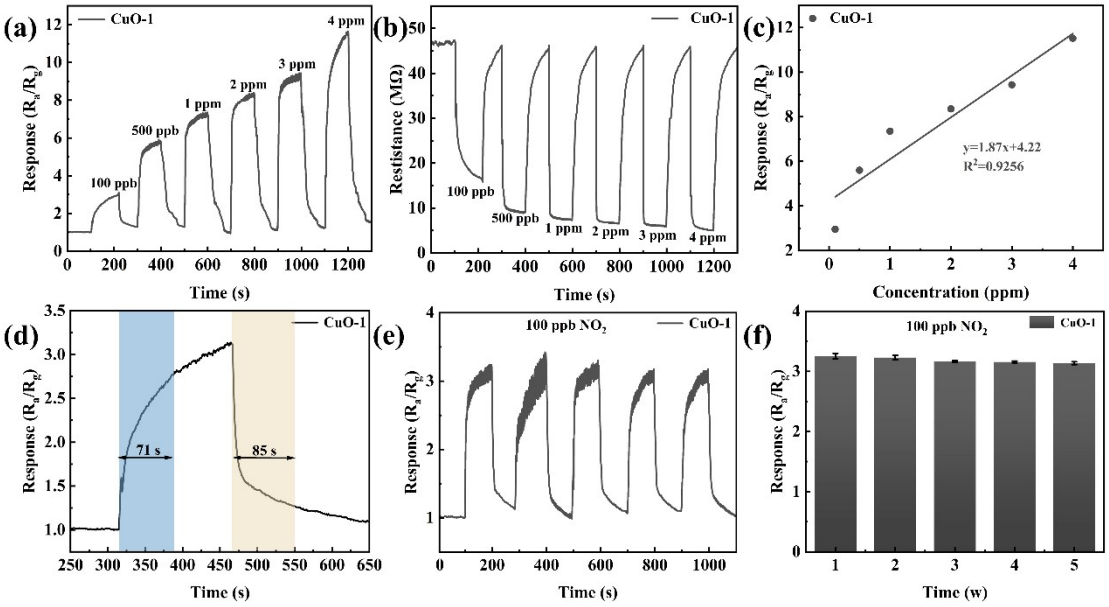

Fig. S7 (a) Dynamic response-recovery curves of the CuO-1 sensor toward NO_2 concentrations ranging from 100 ppb to 4 ppm at 75°C. (b) Dynamic resistance curves of the CuO-1 sensor toward NO_2 concentrations ranging from 100 ppb to 4 ppm at 75°C. (c) Linear fitting relationship between NO_2 concentration and response values of the CuO-1 sensor at 75°C. (d) Instantaneous response-recovery curve of CuO-1. (e) Repeatability curve of five cycles of CuO-1. (f) Long-term stability with perfect curve of CuO-2 to 100 ppb NO_2 at 75°C.

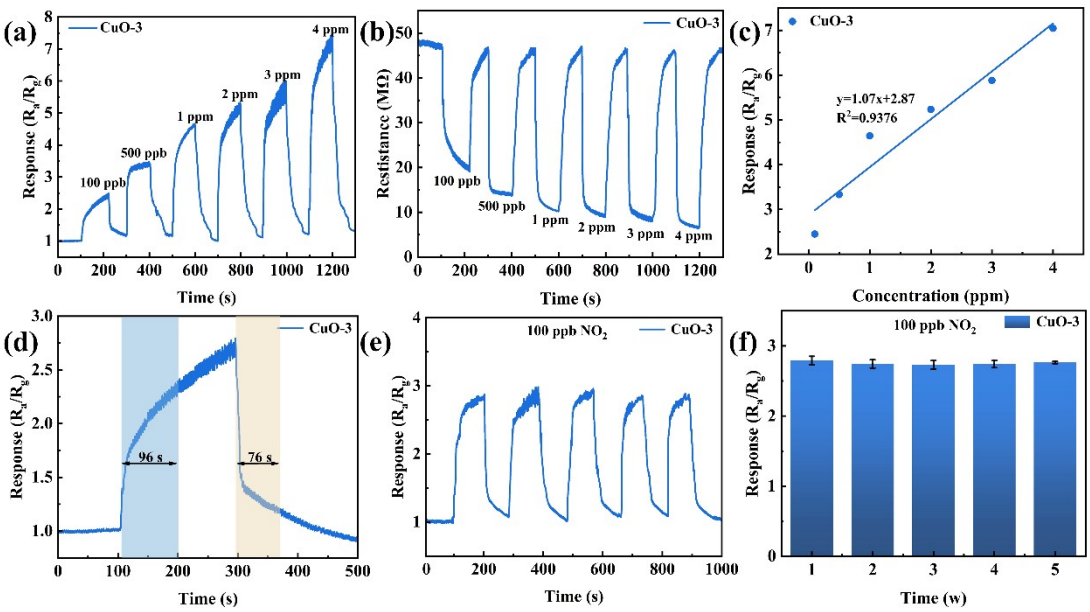

Fig. S8 (a) Dynamic response-recovery curves of the CuO-3 sensor toward NO_2 concentrations ranging from 100 ppb to 4 ppm at 75°C. (b) Dynamic resistance curves of the CuO-3 sensor toward NO_2 concentrations ranging from 100 ppb to 4 ppm at 75°C. (c) Linear fitting relationship between NO_2 concentration and response values of the CuO-3 sensor at 75°C. (d) Instantaneous response-recovery curve of CuO-3. (e) Repeatability curve of five cycles of CuO-3. (f) Long-term stability with perfect curve of CuO-3 to 100 ppb NO_2 at 75°C.

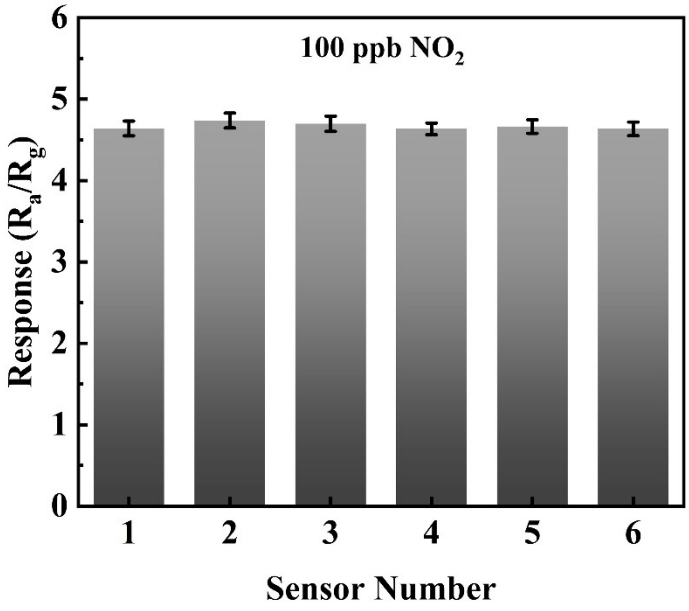

Fig. S9 Response values and error bars for six independently prepared CuO-2 sensors at 75°C for 100 ppb NO_2.

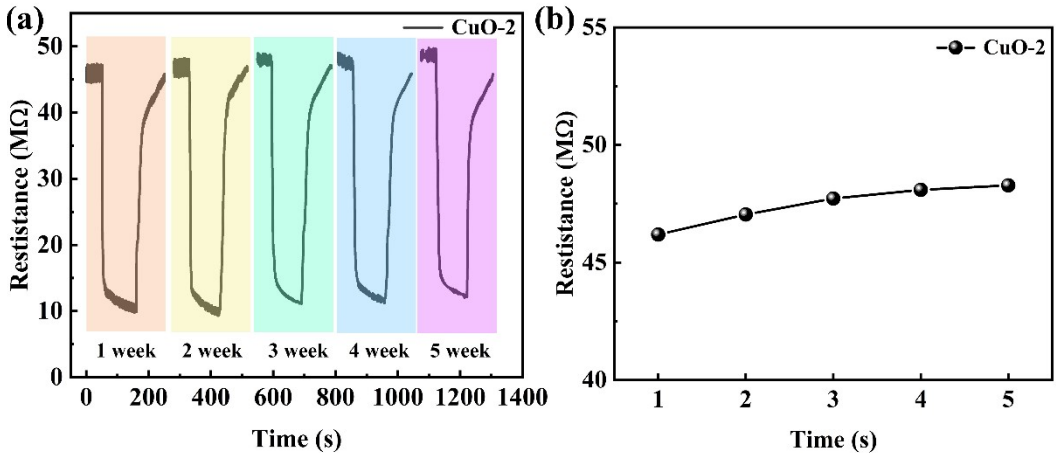

Fig. S10 (a) Dynamic resistance curve of the CuO-2 sensor at 75℃ for 100 ppb NO_2 over five consecutive weeks. (b) Trend of base resistance in CuO-2 sensor at 75℃ for 100 ppb NO_2 over five weeks.

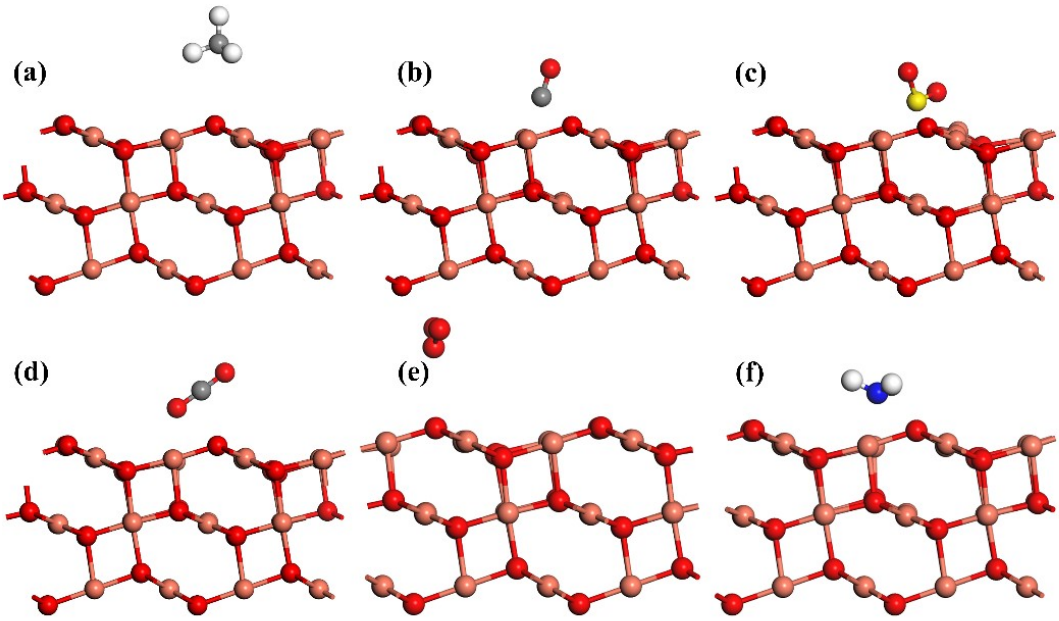

Fig. S11 Optimized adsorption configuration of (a) CH_4, (b) CO, (c) SO_2, (d) CO_2, (e) O_3, and (f) NH_3 on CuO surfaces with oxygen vacancies.

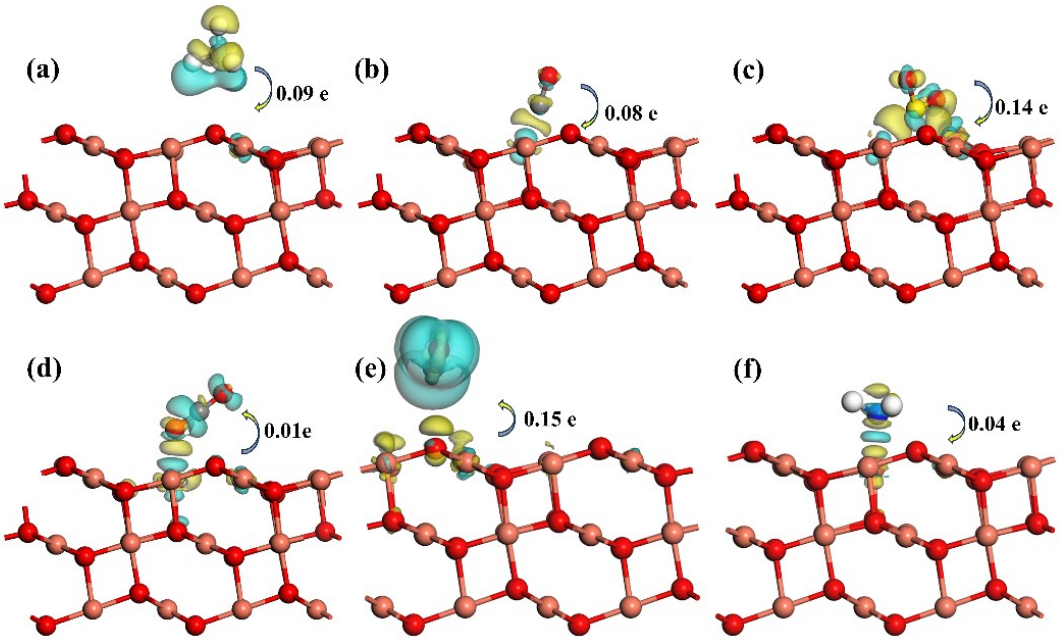

Fig. S12 The charge density difference plot of (a) CH_4, (b) CO, (c) SO_2, (d) CO_2, (e) O_3, and (f) NH_3 interaction with the CuO plane with oxygen vacancies, where blue and yellow represent positive and negative changes in charge densities (e/Bohr3), respectively. A positive charge change (blue) corresponds to a depletion of Bader charge, while a negative charge change (yellow) indicates an accumulation of Bader charge.

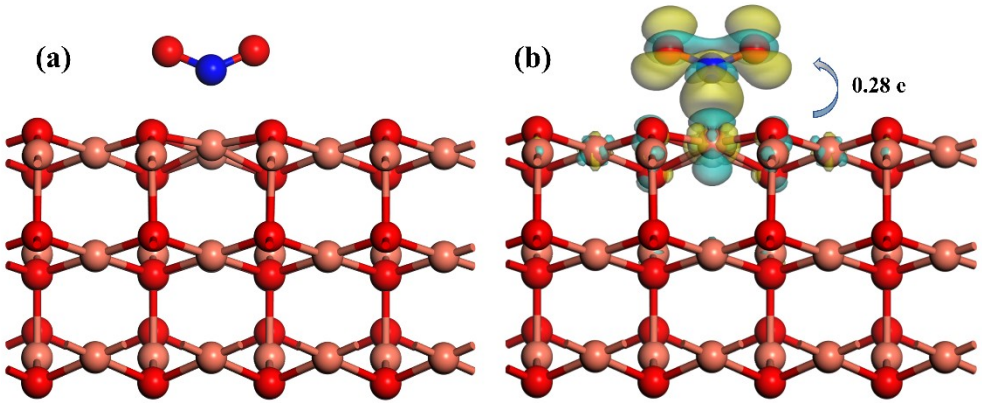

Fig. S13 (a) Optimized adsorption configuration of NO_2 on the CuO (111) plane. (b) The charge density difference plot of NO_2 interaction with the CuO (111) plane.

References:

1. R. Xue, L. Yu, M. Gong, C. Zhang, S. Li, S. Yang, X. Xiao, N. Nan, C. Li and X. Fan, *Sensors and Actuators B: Chemical*, 2025, **441**, 138047.